Journal of Electronic Materials (2022) 51:6397–6409
https://doi.org/10.1007/s11664-022-09874-3

ORIGINAL RESEARCH ARTICLE

Investigation of Diode Parameters of Photoconductive and Photovoltaic *p*-Type Si/Ge-Doped WO_x Heterojunction

Fatih Ünal[1]

Received: 23 April 2022 / Accepted: 5 August 2022 / Published online: 26 August 2022
© The Minerals, Metals & Materials Society 2022

Abstract

The physical vapour deposition technique was employed to deposit Ge-doped WO_x thin film on a *p*-type Si wafer. Structural analyses obtained from x-ray diffraction (XRD) spectroscopy indicate that the deposited thin film has four phases, namely $Ge_{0.04}WO_3$, GeO_2, WO_3 and W_5O_{14}. The thickness of the thin film was measured as 435 nm from a cross-sectional scanning electron microscopy image. A 5.7% dopant ratio of Ge was determined from the energy-dispersive x-ray (EDX) spectrum. The current–voltage (I–V) characteristics of the heterojunction were investigated under dark conditions and several light intensities. The diode ideality factor (n), series resistance (R_s), barrier height (ϕ_b) and reverse saturation current (I_0) were determined using conventional and Cheung–Cheung methods. The values of n decreased to 1.7 and I_0 increased from 7.31×10^{-8} A to 4.7×10^{-5} A with increasing light intensity. Additionally, the photocurrent (Iph), photoresponsivity (R) and photosensitivity (S) of the heterojunction were examined, and it was observed that these values increased with the increase in light intensity, in particular under forward bias. The photovoltaic properties of the heterojunction were also evaluated, and the maximum fill factor (FF) value of 0.266 was observed at 100 mW cm^{-2} light intensity.

Keywords Photodiode · photovoltaic · photoconductivity · photoresponsivity · heterojunction · PVD · metal oxide · dopant

Introduction

Nanotechnology plays a critical role in the fabrication and enhancement of products in science and technology. In particular, it is capable of producing an ultra-high-quality structure with controllable properties at the desired morphology, size and shape.[1–5] For instance, thin-film technology, such as epitaxial growth, electrochemical deposition, spin coating, thermal evaporation and magnetron sputtering, is an important and widely used technique for the fabrication of more effective photodiodes and photovoltaic devices.[6–14] Among these techniques, magnetron sputtering enables co-deposition of materials by superior control of purity, film thickness and surface morphology.

There is high demand for organic and inorganic materials in applications such as photonics and flexible electronics.[15–17] Among these materials, transparent metal oxides have been widely used in optoelectronic devices due to their unique optical and electrical properties. Whilst ZnO, TiO_2, CdO, SiC and NiO may be preferred for many optoelectronic applications,[18–22] tungsten oxides have garnered a great deal of interest due to their unique properties in applications ranging from electro-chromatic,[23] sensor[24,25] and high-quality interconnections,[26] to optoelectronic, photovoltaic and energy storage devices, and its products can be altered by several techniques during the deposition process.[27] Additionally, metal oxide features can be modified by doping or tuning the chemical composition by another element.[8,28] For instance, germanium (Ge) has been used as a dopant in metal oxides to improve their performance in various applications.[15,28–32] Additionally, some studies have reported the use of tungsten as a dopant material—for example, W doped to TiO_2,[33] $BaSrTiO_3$[34] and SnO_2 to improve the structural, optical, electrical and photocatalytic performance. Other examples of the use of W as a dopant can also be found; for instance, W is doped to VO_2[35] to reduce to the critical temperature for metal–insulator transition. The geometric and electronic properties of the W-doped Ge cluster were investigated by density functional theory. It was found that W-Ge and their oxides can be used as dopants, semiconductor or

✉ Fatih Ünal
fatih.unal@giresun.edu.tr

[1] Central Research Laboratories GRUMLAB, Giresun University, 28200 Giresun, Turkey

insulator layers, or also doped to another in optoelectronic applications.

Hence, an Al/Si/WO_x:Ge(5.7%)/Ag heterojunction was fabricated by doping Ge into tungsten oxide by the co-deposition technique under a vacuum environment. Structural and morphological investigations were performed, and the I–V characteristic curve was determined under dark and various light intensities to provide an alternative for optoelectronic circuit elements.

Materials and Methods

The physical vapour deposition (PVD) technique was employed for the fabrication of a heterojunction diode, as shown in the structural diagram in Fig. 1. Firstly, a *p*-type Si substrate with an Al support layer was cleaned using acetone, methanol and distilled water, respectively, in an ultrasonic bath and then dried with nitrogen gas. Afterwards, a Nanovak magnetron sputtering system (Model: NVTS-400) which has two RF and one DC magnetron sputter head, was used to deposit Ge-doped WOx thin film by the co-deposition technique. The base pressure of the deposition system was approximate 0.133 kPa during the deposition and was about 0.266 kPa under a 0.666 kPa Ar gas environment. Applied power and Ar pressure are generally used to alter the deposition rate of target materials so the film thickness and doping material ratio can be controlled during the co-deposition process. The deposition rate of sputtered materials was controlled by a quartz crystal thickness monitor. Hence, the deposition rate of the W target with a purity of 99.99% percent was kept at 1.6 Å s^{-1} by applying DC voltage (395 V, 250 mA). Besides this, an RF power-supply-connected magnetron sputter source was used for the co-deposition of Ge (99.99% percent purity) with a deposition of 1.2 Å s^{-1} by applying 55 W sputtering power. The co-deposition process was carried out up to reach desired thickness. Fabrication of the heterojunction was finally completed by deposition of Ag Schottky contacts by RF magnetron sputtering with a deposition rate of 1.8 Å s^{-1}. The thickness of the Ag contact was settled at approximately 150 nm.

The phase structure of the heterojunction was examined by x-ray diffraction (XRD) (G.N.R. Europe 600 diffractometer) using Cu-Kα (1.5418740 Å) radiation from 10 ° to 80 °. Scanning electron microscopy (SEM) (FEI Versa 3D DualBeam) was employed to examine the surface morphology of the deposited film. Energy-dispersive x-ray spectrometry (EDX) was performed to determine the elemental composition of the heterojunction. Additionally, the doping ratio of Ge in thin film was obtained from SEM–EDX analysis. The deposited film thickness was also determined from a cross-section SEM image of the fabricated device.

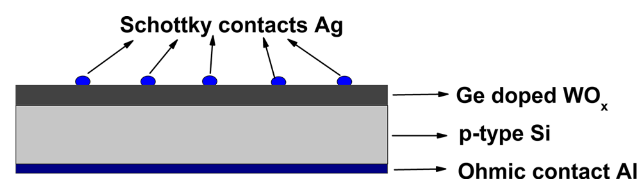

Fig. 1 Structural diagram of the Al/Si/WO_x:Ge(5.7%)/Ag heterojunction.

I–V characteristic measurement of the heterojunction was carried out using the FYTRONIX Solar Simulator LS 900 Characterisation System, which is fully automated and controlled by a computer and enables dark and various light I–V characterisation.

Results and Discussion

Phase Structure, Surface Morphology and Elemental Composition

The XRD graph of Ge-doped WO_x thin film is illustrated in Fig. 2a, and the high-magnification XRD spectrum of the low-intensity region (labelled in Fig. 2a) is demonstrated in Fig. 2b. The amorphous to polycrystalline phase structure of the thin film is clearly seen in Fig. 2a and b, and the Ge-doped WO_x thin film has obvious phase peaks which can be assigned to $Ge_{0.04}WO_3$, GeO_2, WO_3 and W_5O_{14} phases, for which the standard spectrums are shown in Fig. 2c. Also, details of the crystal parameters of these phases are given in Table I.

The structural parameters including particle size (D), dislocation density (δ) and lattice strain (ε) were calculated from the most dominant (sharp) peaks in the spectrum and are given in Table II. The particle size is calculated by the Scherrer equation, $D = 0.90\lambda/\beta cos\theta$, where λ is the wavelength of the incident x-rays (1.5418740 Å for Cu-Kα), β is the full width at half maximum (FWHM) and θ is the Bragg angle. The dislocation density is calculated with the Williamson and Smallman formula as $\delta = 1/D^2$ and the equation $\varepsilon = \beta\cos\theta/4$ is used to obtain lattice strain. The low dislocation density and lattice strain and large particle size indicates that the film structure is properly crystallised.[36,37]

The surface morphology of Ge-doped WO_x thin film deposited on a *p*-type Si wafer by PVD was investigated by SEM, and the SEM images are illustrated in Fig. 3a. The PVD technique leads to a uniform surface profile with some visible grain boundaries. The thin film has a smooth surface without cracks or pores, as shown in Fig. 3a. As illustrated in Fig. 3b, heterojunction layers are distinguishable and film thickness was measured as 435 nm from the cross-section SEM image.

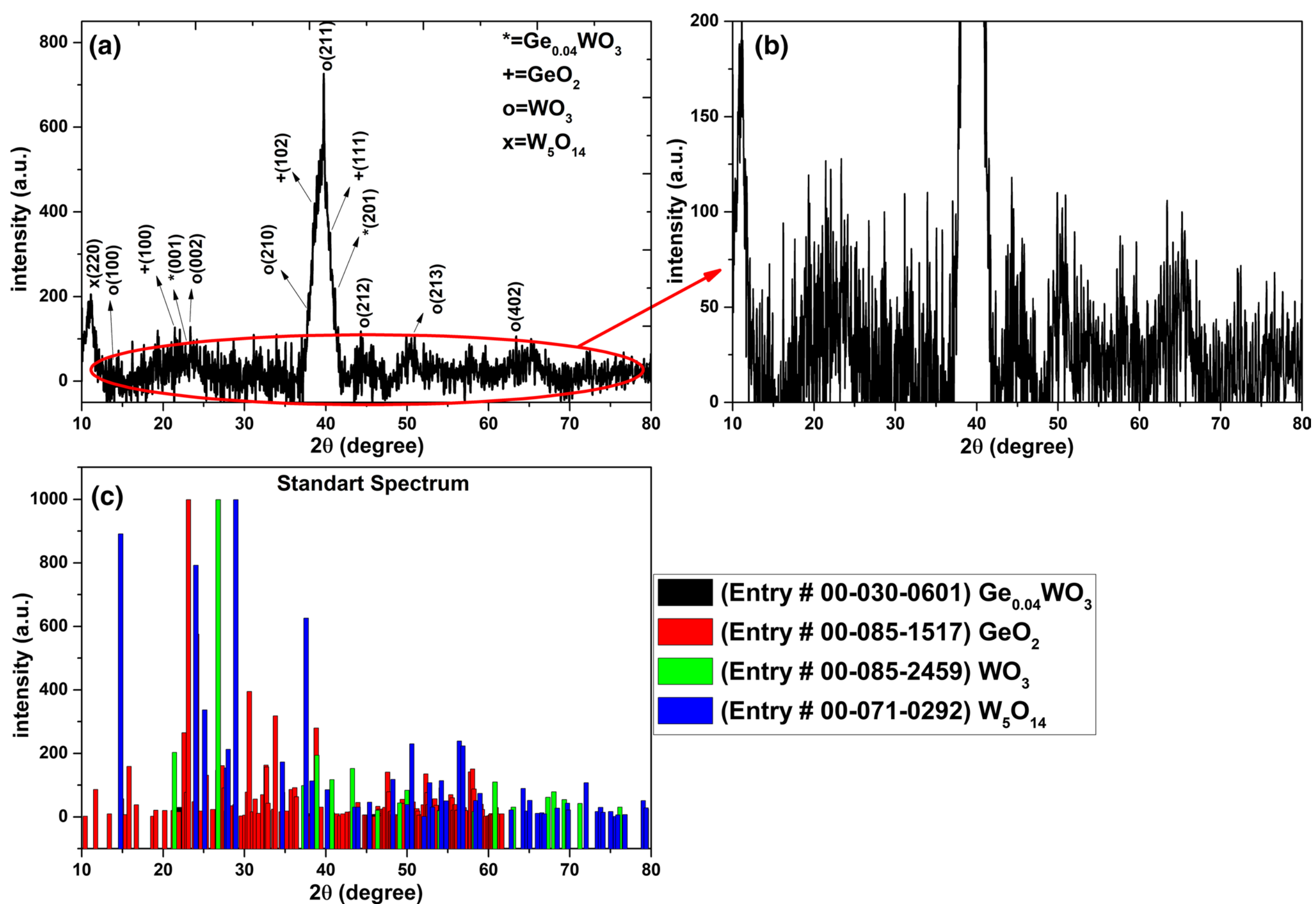

Fig. 2 (a) The phase structure of Ge-doped WO_x thin film, (b) high magnification XRD spectrum of the selected area of Fig. 2(a), (c) standard XRD spectrum.

Table I Crystal parameters of detected phases from XRD measurement

Entry #		$Ge_{0.04}WO_3$ 00-030-0601	GeO_2 00-085-1517	WO_3 00-085-2459	W_5O_{14} 00-071-0292
Crystal system		Tetragonal	Hexagonal	Hexagonal	Tetragonal
Space group		–	P3221(154)	P63mcm(193)	P-421 m(113)
Unit cell dimensions (Å)	a	5.30	4.85	7.32	23.33
	b	3.88	–	–	–
	c	–	5.59	7.66	3.80
Cell volume ($Å^3$)		108.96	114.18	356.01	2066.66
Z		–	3	6	8

SEM–EDX mapping was employed to characterise the chemical composition of the deposited film. Figure 4d indicates that the thin film contains elements of W, Ge and O. In Fig. 4a–c, it can be clearly seen that all the W, Ge and O are homogeneously distributed. The percentage atomic content is 71.75% W, 11.24% Ge and 17.01% O, and the percentage of elemental weight is demonstrated in the inset of Fig. 4d. It is clear that W and Ge have 92.5% and 5.7% elemental weight in the deposited film. Additionally, the EDX spectrum indicates that the film has 1.9% wt O. Since the deposited thin film has contacted the atmosphere, the oxidation process has taken place naturally. The results of the EDX analysis support the results of the XRD analysis. Hence, the heterojunction will be labelled Al/Si/WO_x:Ge(5.7%)/Ag.

Table II Structural parameters of phases that occur in the thin film layer

2-theta	Phase	hkl	FWHM(β)	Particle size (D) (nm)	Lattice strain (ε)	Dislocation density (δ) (nm^{-2})
22,85	$Ge_{0.04}WO_3$	001	4.52	1.72	1.10	3.93×10^{17}
41,13		201	1.52	4.89	0.35	4.17×10^{16}
21,16	GeO_2	100	6.26	1.24	1.53	6.42×10^{17}
38,63		102	2.2	3.40	0.51	8.60×10^{16}
40,45		111	1.48	5.03	0.34	3.93×10^{16}
13,93	WO_3	100	3.04	2.59	0.75	1.48×10^{17}
23,36		002	2.7	2.88	0.66	1.20×10^{17}
37,55		210	0.66	11.39	0.15	7.69×10^{15}
39,35		211	2.48	3.01	0.58	1.09×10^{17}
44,12		212	–	–	–	–
52,3		213	–	–	–	–
63,44		402	–	–	–	–
10,94	W_5O_{14}	220	1.28	6.17	0.31	2.61×10^{16}

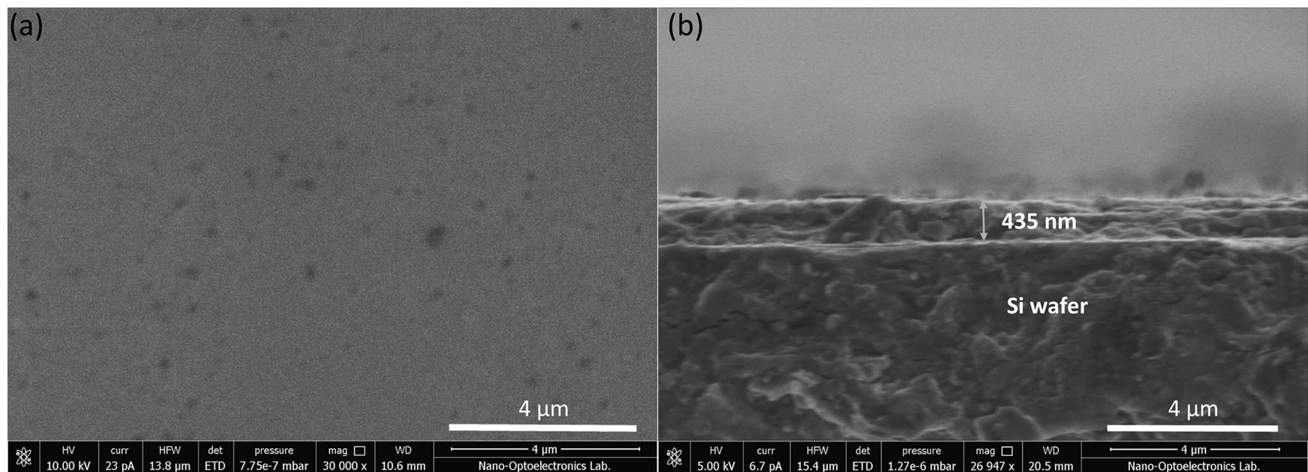

Fig. 3 (a) SEM image of Ge-doped WO_x thin film surface, (b) represents the cross-section SEM image of the heterojunction.

Electrical Characterisation

In this work, 5.7% Ge-doped WO_x thin film was deposited on a *p*-type Si wafer by PVD technique and afterwards Ag Schottky contacts were grown on the film surface. The synthesised heterojunction actually formed as a metal–insulator–semiconductor (MIS) type Schottky barrier diode (SBD) structure. Since the thin film deposited on the semiconductor layer (*p*-type Si) formed as a metal oxide (supported by XRD and EDX analyses), the metal contacts were taken and formed the MIS structure. Here, the metal oxide layer is considered an insulating layer, and similar studies are available in the literature.[38–41] The I–V characteristics of the Al/Si/WO_x:Ge(5.7%)/Ag heterojunction were investigated under dark and various illumination intensities ranging from 20 mW cm^{-2} to 100 mW cm^{-2} between ± 2 V applied voltage ranges at room temperature. Based on the current–voltage mechanism of the metal–insulator–semiconductor Schottky barrier diode, electrical characteristics of the diode including diode ideality factor, barrier height and series resistance can be calculated by different methods.[42,43]

In the conventional method, the relationship between the current and voltage is determined by thermionic emission theory with the following equation[44–46]:

$$I = AA^{*}T^{2}\exp\left(-\frac{q\varnothing_b}{\mathrm{kT}}\right)[\exp\left(\frac{q(V-\mathrm{IR}_s)}{\mathrm{kT}}\right)-1] \quad (1)$$

where A is the active diode area, A^* is the Richardson constant (32 A cm^{-1} K^2 for *p*-type Si), q is the electron charge, ϕ_b is the barrier height, k is the constant, T is the temperature (Kelvin), V is the applied voltage and R_s is the series

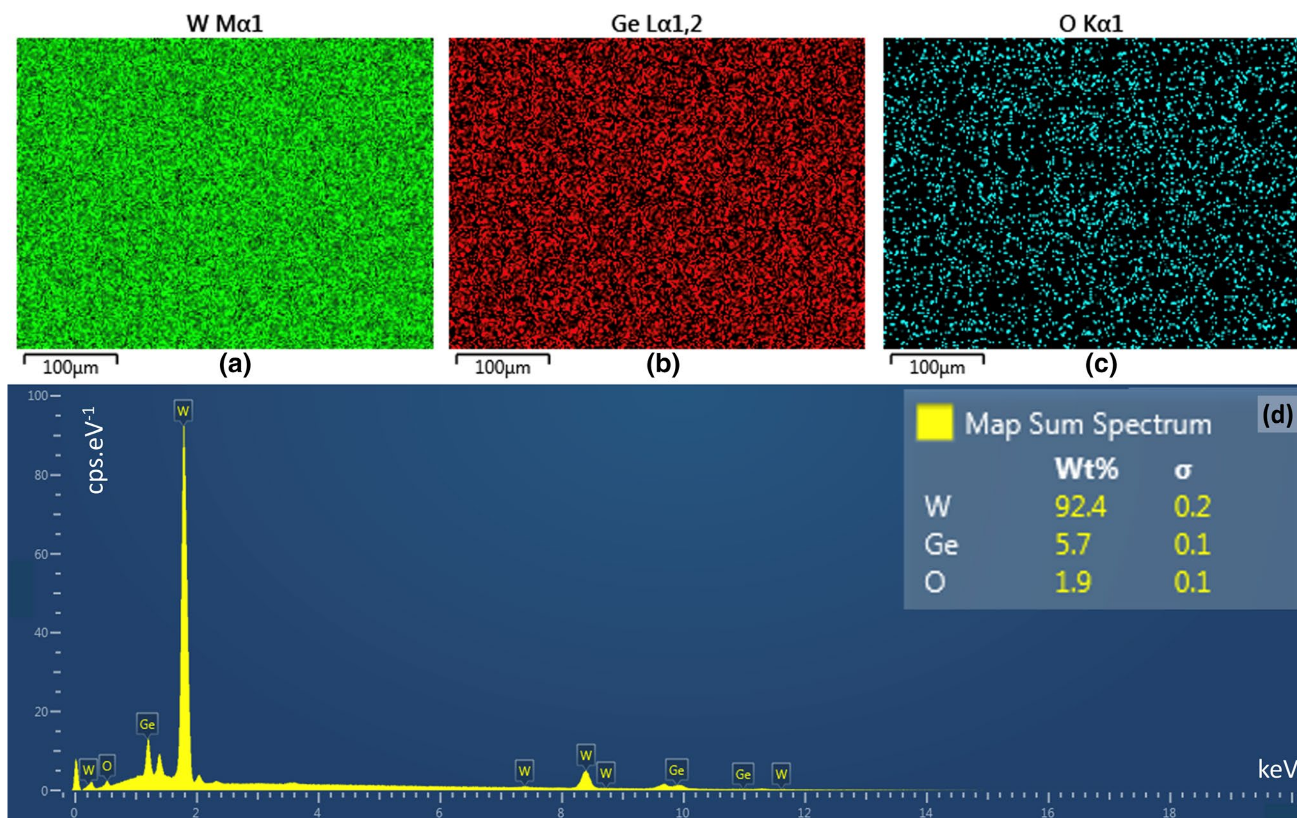

Fig. 4 SEM–EDX elemental mapping of (a) tungsten, (b) germanium, (c) oxygen and (d) EDX spectrum of the thin film surface.

resistance. In the case of $V - \mathrm{IR}_s >> 3\mathrm{kT}$ Eq. 1 is formed as in Eq. 2

$$I = I_0 \exp\left(\frac{\mathrm{qV}}{\mathrm{nkT}}\right) \tag{2}$$

where

$$I_0 = AA^* T^2 \exp\left(-\frac{q\varnothing_b}{\mathrm{kT}}\right) \tag{3}$$

After taking the logarithm of both sides of Eq. 2 and the derivative concerning V, the diode ideality factor (n) can be given by

$$n = \frac{q}{\mathrm{kT}} \frac{dV}{d\ln(I)} \tag{4}$$

The ideality factor (n) can be calculated from the slope of the linear region of the ln(I) versus V graph. Additionally, the reverse saturation current (I_0) is derived from the point where the linear region of the graph of ln(I) versus V intersects ln(I). After defining the I_0, the barrier height is calculated using Eq. 5.

$$\phi_b = \frac{kT}{q} \ln\left(\frac{AA^* T^2}{I_0}\right) \tag{5}$$

The Cheung–Cheung method is the second method used to determine the ideality factor, barrier height and series resistance, using the Cheung–Cheung functions[47] which are given by the following equations:

$$\frac{dV}{d\ln(I)} = \mathrm{IR}_s + \frac{\mathrm{nkT}}{q} \tag{6}$$

$$H(I) = V - \frac{\mathrm{nkT}}{q} \ln\left(\frac{I}{AA^* T^2}\right) \tag{7}$$

$$H(I) = IR_s + n\varnothing_b \tag{8}$$

By considering the low and medium bias region of the I–V plot, the $\frac{dV}{d\ln(I)}$ versus I and H(I) versus I graphs are plotted. And from the slope of the $\frac{dV}{d\ln(I)}$ versus I graph and the value where the curve cuts the y-axis using other constants, R_s and n are calculated, respectively. In addition, it is possible to determine the ϕ_b by using the point where the curve

comes from the H(I) versus I graph, cutting the y-axis and the n value. Also, the slope of this curve can be used to define the R_s value. Furthermore, from the graph of junction resistance ($Rj = \frac{\partial V}{\partial I}$) versus V, the series resistance R_s of the junctions can be determined.[48,49]

Figure 5 illustrates the I–V characteristic curve of the Al/Si/WO_x:Ge(5.7%)/Ag heterojunction, and it can be clearly seen that the heterojunction shows rectifying characteristics and its photoconductivity increases with the increase in the intensity of light falling on it. Semi-logarithmic I–V characteristics of the Al/Si/WO_x:Ge(5.7%)/Ag heterojunction are demonstrated in Fig. 6, and asymmetry can be observed between the reverse and forward bias voltages, especially in the dark region. In addition, it is seen that the linear region of the curves drops between 0.05 and 0.3 V under forward bias and the series resistance effect appears, while voltage increases from this value. At the same time, non-saturation behaviour can be observed under reverse bias, and this can be explained primarily by the interface states of the WO_x:Ge(5.7%) layer and metal, and image-force lowering by the barrier height.[50] Photons with higher energy than the forbidden band gap energy under illumination provide the formation of new electron–hole pairs in the depletion region of the semiconductor. The structure is stressed under the external electric field, and the electron–hole pairs generated are forced to separate by a strong internal electric field at the grain boundary. And thanks to the electric field, electrons are quickly swept away and photoconductivity is increased. Hence, the photoconductivity becomes more distinguishable in the range of 1 V to 2 V.

In Fig. 7, ln(I) versus ln(V) is plotted to illustrate in greater detail the current conduction mechanism of the Al/Si/WO_x:Ge(5.7%)/Ag heterojunction in the forward bias region. It is clear that three regions are available under both dark and light intensity as illustrated in Fig. 7. The region where the ln(V) value is between −2.5 and −1.5 falls into the ohmic region of the first region. This is because the amount of current produced in the heterojunction is greater than the current generated by the injected free carriers.[51–54] The region with ln(V) values between −1.5 and 1 is the second region, and it refers to the space-charge-limited current (SCLC) region controlled by traps. The reason for these traps is the increased injection of electrons from the metal to the film with increasing applied voltage. The increase in the number of injected electrons leads to the filling of the traps and increases the space charges.[55–57] The third region

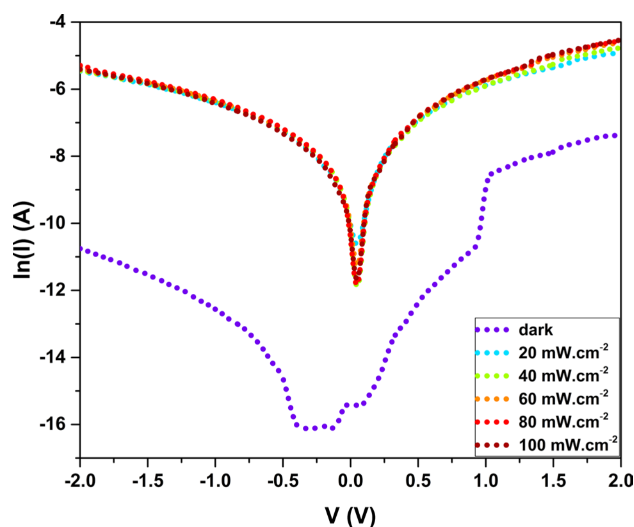

Fig. 6 Semi-logarithmic I–V characteristic curve of the Al/Si/WO_x:Ge(5.7%)/Ag heterojunction.

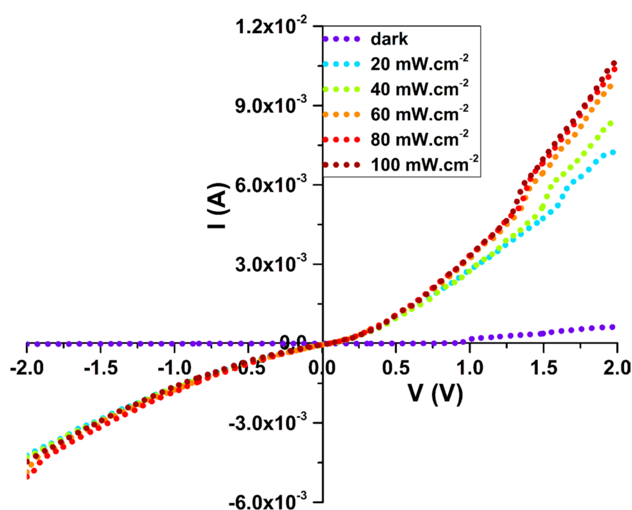

Fig. 5 I–V characteristic curve of the Al/Si/WO_x:Ge(5.7%)/Ag heterojunction.

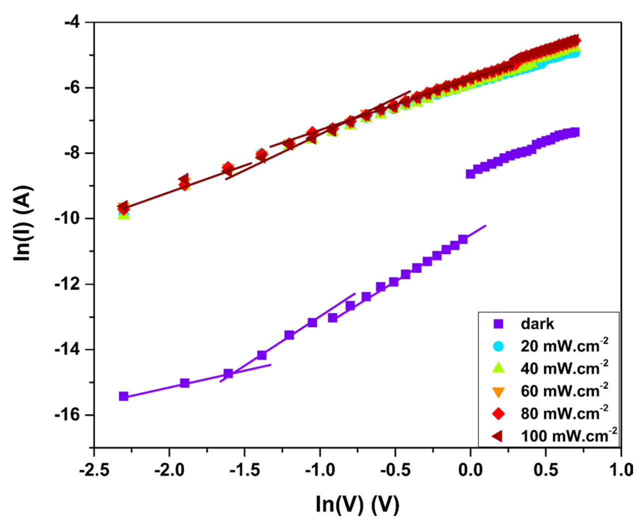

Fig. 7 Double logarithmic plots of the Al/Si/WO_x:Ge(5.7%)/Ag heterojunction.

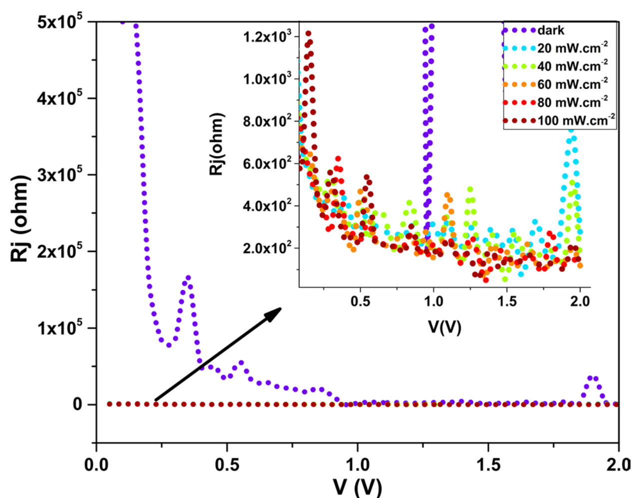

Fig. 8 Forward bias Rj–V graph of the Al/Si/WO_x:Ge(5.7%)/Ag heterojunction.

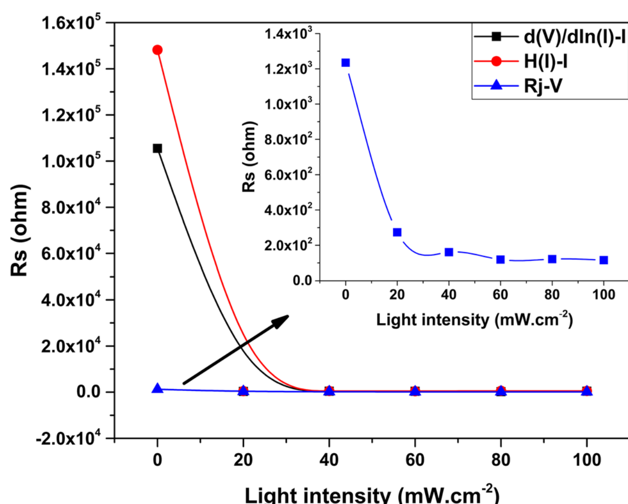

Fig. 9 The relationship of evaluated R_s values with different methods against the light intensity. Inset represents the high magnification graph of R_s values calculated with the Rj–V curve.

occurs at a high bias region and has a strong injection area. In this region, electrons escape from traps and contribute to the SCLC.[44,55,58,59]

Figure 8 presents the Rj–V graph of the Al/Si/WO_x:Ge(5.7%)/Ag heterojunction under the forward bias condition. It is evident that junction resistance is high at low voltage, and with higher voltage, it decreases. Additionally, the increase in the current depending on the carrier concentration with the increase in light intensity leads to a drop in the junction resistance. It is seen that the Rj values fluctuate and decrease with increasing applied potential. This can be attributed to the disordered charge distribution.

Figure 9 shows changes in the series resistance values calculated from the curves of Rj–V, d(V)/dln(I)–I and H(I)–I, depending on light intensity. It is obvious that all R_s values calculated with the three methods decreased exponentially with the increasing intensity of light. R_s values are determined as 1.23×10^3 Ω, 1.05×10^5 Ω and 1.5×10^5 Ω from the Rj–V, d(V)/dln(I)–I and H(I)–I curves under dark conditions, respectively. Also, under 100 mW cm^{-2} illumination, these R_s values drop to 1.15×10^2 Ω, 4.29×10^2 Ω and 5.29×10^2 Ω, respectively. The reason for the decrease in R_s values with increasing light intensity is related to increasing photoconductivity.

n and ϕ_b , depending on the light intensity, were calculated and are respectively presented in Fig. 10a and b. Values of n and ϕ_b calculated by both methods show similar behaviour against the change in light intensity. While n values determined from the d(V)/dln(I)–I curve are between 2.79 and 1.70, the H(I)–I curve yielded ϕ_b values between 1.07 eV and 0.67 eV. Additionally, n and ϕ_b values obtained from ln(I)–V curves take values between 5.69 and 4.16, and 0.73 eV and 0.56 eV, respectively. The n and ϕ_b values have an opposite correlation, as shown in Fig. 10a and b. Both barrier height and ideality factor values are coherent with those in the literature. Kocyigit et al. reported a similar finding regarding the relationship between ϕ_b and n.[60] Additionally, n values calculated by both methods are far from ideal diode values ($n=1$). The reasons for this are the potential drop across the interface layer, natural oxide layer formation, and the overcurrent at the interface state which is between the series resistance and Al/Si/WO_x:Ge(5.7%)/Ag layers.[48,61] Another reason for the high n value could be the non-homogeneous distribution of charges at the interface layer.[62] The n values showed a fluctuating change with the increase in light intensity. This can be explained by the rearrangement and reconstruction of the structure at the molecular level by increasing the light intensity.

In Fig. 11 the graph of the reverse saturation current, I_0, versus light intensity is presented. It is obvious that the reverse saturation current increases with light intensity and reaches its maximum value at 80 mW cm^{-2} and then drops again. The reason for this trend is that photo-generated carriers of light activate recombination at the interface. While the I_0 value in a dark environment is 7.31×10^{-8} A, it increases to 4.69×10^{-5} A at 80 mW cm^{-2} illumination. It is remarkably clear that reverse saturation current increases approximately 1000-fold, and it means that the designed heterojunction is highly sensitive to light. The increase in I_0 with light intensity can be attributed to a decrease in the value of R_s.

The rectification ratio (r) is a vital parameter for rectifier diodes and is calculated by the formula $r = I_f/I_r$.[63,64] Here, I_f and I_r refer to currents under forward bias and reverse bias, respectively. r values were calculated at voltage of 0.5 V, 1 V, 1.5 V and 2 V under different light intensity, and the results are presented in Fig. 12. It is clear that r values at certain voltages decrease exponentially with increasing light

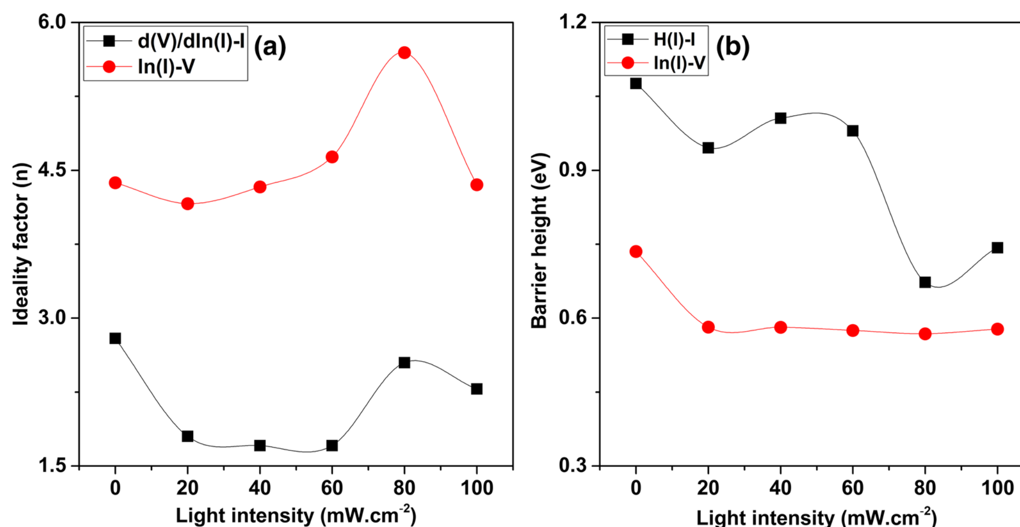

Fig. 10 (a) Diode ideality factor, (b) barrier height of the Al/Si/WO_x:Ge(5.7%)/Ag heterojunction against the intensity of light.

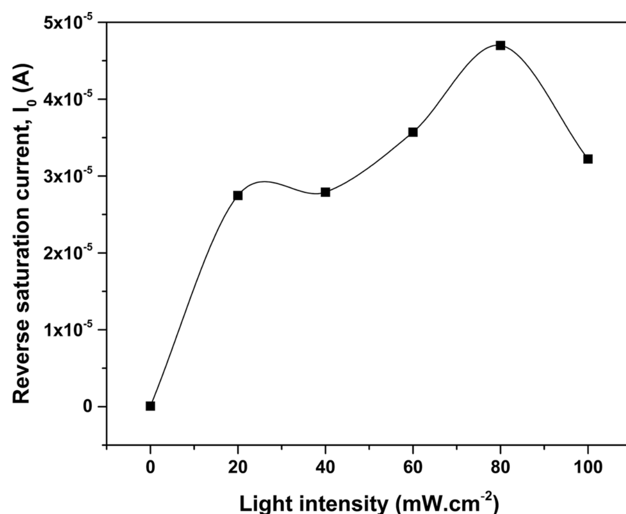

Fig. 11 The plot of reverse saturation current versus light intensity.

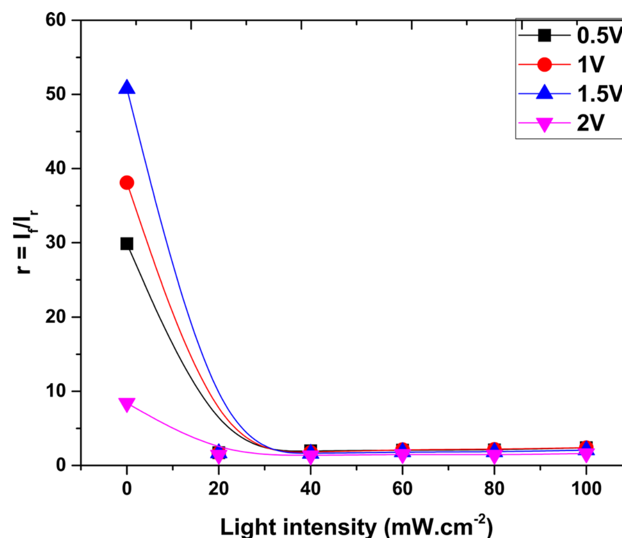

Fig. 12 Rectification ratio (r) of the Al/Si/WO_x:Ge(5.7%)/Ag heterojunction plotted as a function of light intensity at certain bias voltages.

intensity, which is in agreement with the literature.[65,66] The highest *r* value under dark conditions was observed at a voltage of 1.5 V, and there is no obvious trend between *r* value and applied bias voltage.

In Fig. 13a–d, the changes in photocurrent (Iph) depending on light intensity are evaluated at certain voltages (0.5 V, 1 V, 1.5 V and 2 V) under forward and reverse bias. It is observed that the photocurrent increases proportionately with the light intensity under forward bias conditions, while this increase reaches a peak point at 80 mW cm^{-2} under reverse bias. This can be explained by the radial change in intensity which alters the photoabsorption.[66] Furthermore, it is seen that Iph increases with increasing bias voltage, and the Iph under forward bias is higher than the Iph under reverse bias at all illuminations, which promotes the nature of the photodiode.

The photoresponsivity (R) value of the fabricated diodes can be calculated with a following equation:

$$R = \frac{I_{\text{ill}} - I_{\text{dark}}}{P_{\text{inc}}.A} \tag{9}$$

where I_{ill} is the current under illuminated conditions, I_{dark} refers to the dark current, P_{inc} is the incident light power and A is the contact area of the diode ($A = 7.85 \times 10^{-7}$ m^2). The photoresponsivity plots of the fabricated Al/Si/

WO_x:Ge(5.7%)/Ag heterojunction at certain bias voltage values ($\pm 0.5, \pm 1, \pm 1.5$ ve ± 2 V) against illumination intensity are given in Fig. 14a–d. For each bias voltage value,

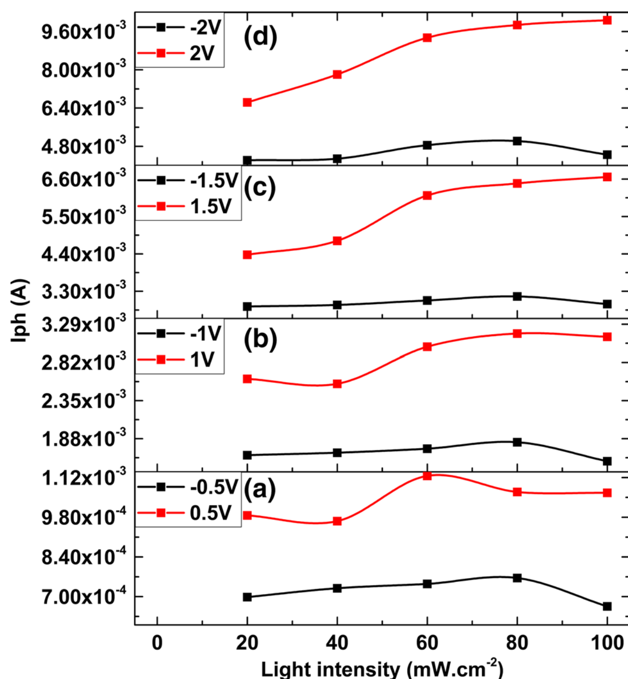

Fig. 13 The plot of photocurrent (Iph) under (a) ± 0.5 V, (b) ± 1 V, (c) ± 1.5 V, (d) ± 2 V against light intensity.

forward responsivity (R_f) and reverse responsivity (R_r) are presented together using two y-axes. It is clear that R_f and R_r are enhanced with illumination intensity and that R_f values are higher than R_r values at all voltage values. In addition, R values rise with increasing bias voltage under both forward and reverse bias.

The photosensitivity (S) of the Al/Si/WO_x:Ge(5.7%)/Ag heterojunction at voltages of $\pm 0.5, \pm 1, \pm 1.5$ ve ± 2 V was determined by the following relation[67]:

$$S = R\frac{T}{V} \tag{10}$$

where S, R, T and V refer to the photosensitivity, photoresponsivity, thickness of the active layer (435 nm for Ge-doped WO_x layer) and applied voltage, respectively. Figure 15a–d illustrates the photosensitivity curves at certain forward and reverse voltage values against the light intensity. Similar to Fig. 14, for each bias voltage value, forward sensitivity (S_f) and reverse sensitivity (S_r) are plotted together by using double y-axes. The similarity of the photosensitivity and photoresponsivity response of the fabricated diode is notable, since photosensitivity increases with increasing light intensity and applied voltage.

Figures 16 and 17 demonstrate the photovoltaic and photodiode region and the photovoltaic parameters (Impp, Isc, Vmpp, Voc ve FF) of the Al/Si/WO_x:Ge(5.7%)/Ag heterojunction under several light intensity values, respectively. The fill factor was calculated with Eq. 11, given by:

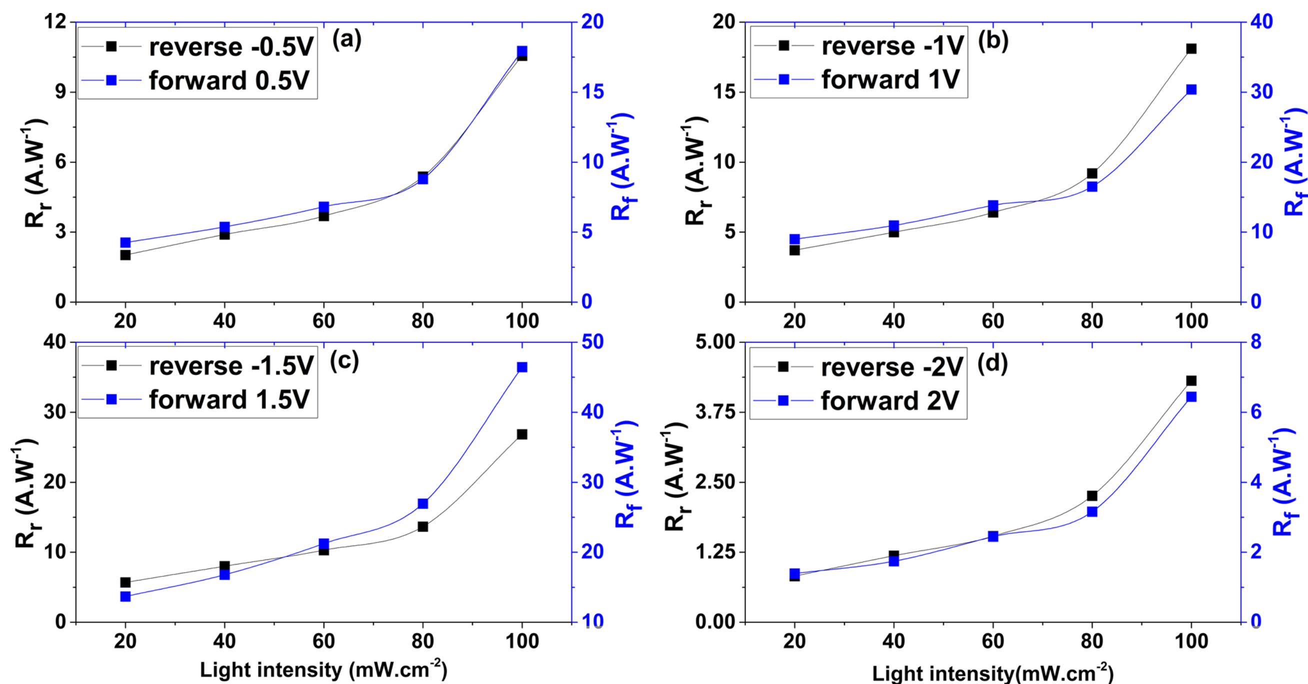

Fig. 14 Photoresponsivity versus light intensity plot of the Al/Si/WO_x:Ge(5.7%)/Ag heterojunction at (a) ± 0.5 V, (b) ± 1 V, (c) ± 1.5 V, (d) ± 2 V.

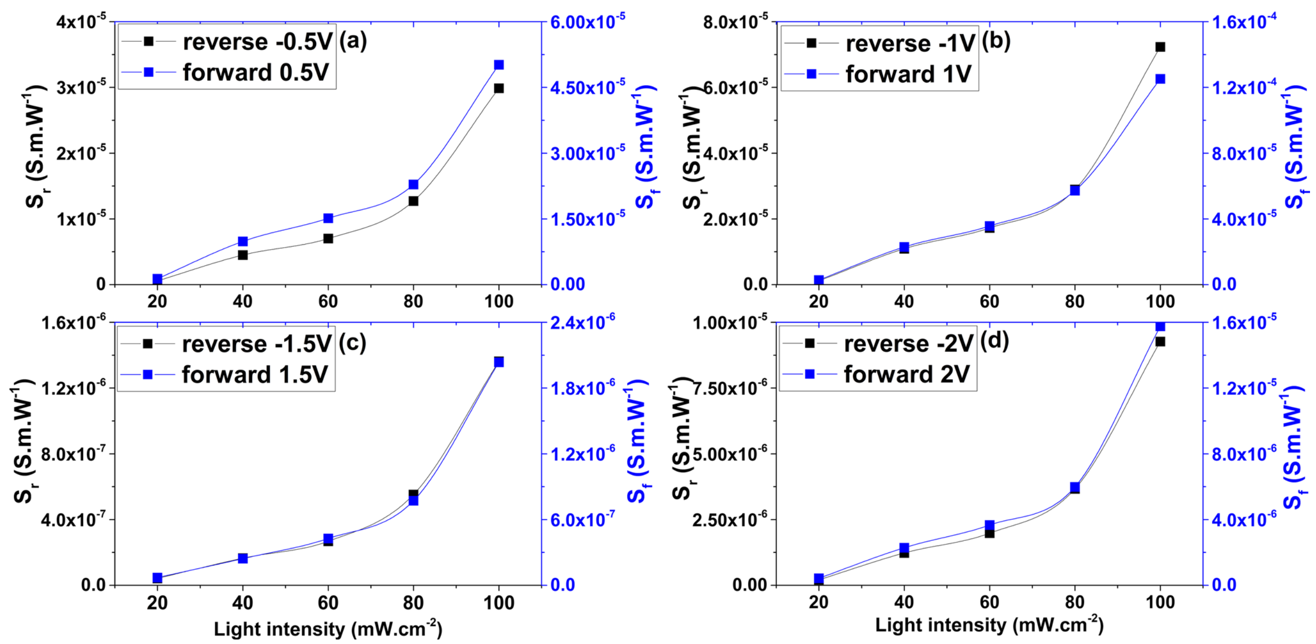

Fig. 15 Photoconductivity sensitivity versus light intensity plot of the Al/Si/WO_x:Ge(5.7%)/Ag heterojunction at (a) ±0.5 V, (b) ±1 V, (c) ±1.5 V, (d) ±2 V.

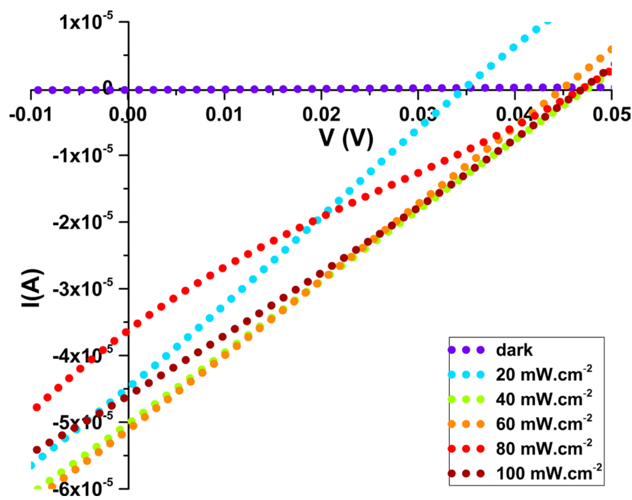

Fig. 16 The plot of the photovoltaic region of the Al/Si/WO_x:Ge(5.7%)/Ag heterojunction under several light intensities.

$$FF = \frac{Impp \times Vmpp}{Isc \times Voc} \tag{11}$$

where Impp is the maximum power point current, Vmpp is the maximum power point voltage, Isc and Voc refers to the short-circuit current and open-circuit voltage, respectively.

The photovoltaic parameters of the Al/Si/WO_x:Ge(5.7%)/Ag heterojunction were determined, and their variation against light intensity is illustrated in Fig. 17a–e. The calculated *FF* values are obtained between

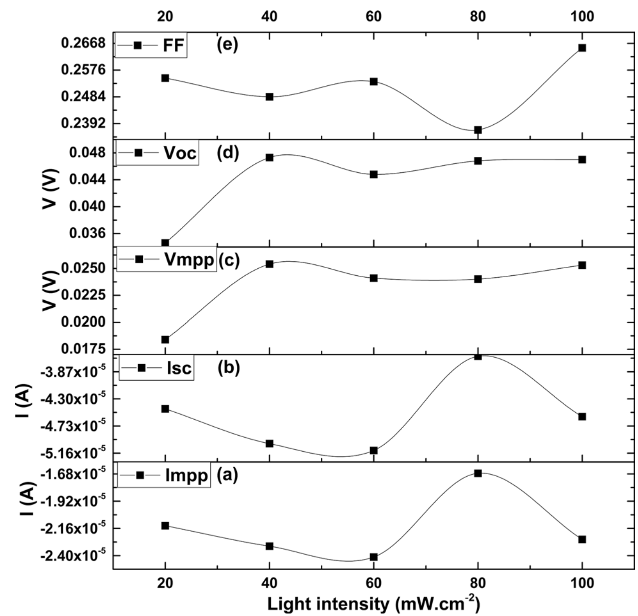

Fig. 17 Changes in the photovoltaic parameters (a) Impp, (b) Isc, (c) Vmpp, (d) Voc and (e) FF against several light intensity values.

0.2668 and 0.2392. It is also seen that *FF* values gradually fluctuate between 20 mW cm^{-2} and 60 mW cm^{-2}, decrease to a minimum value at 80 mW cm^{-2} and reach a maximum value at 100 mW cm^{-2}. Voc and Vmpp are between 0.0336 V and 0.047 V, and 0.0184 V and 0.0253 V, respectively, and they increase with light intensity. *Isc*

values between -5.1178×10^{-5} A and -3.6252×10^{-5} A and Impp values between -2.4129×10^{-5} A and -1.6753×10^{-5} A have similar trends as FF values. As the values of Isc and Impp are in the negative region, their values increase between 20 mW cm^{-2} and 60 mW cm^{-2}, and they decrease to the minimum value at 80 mW cm^{-2} and increase at 100 mW cm^{-2}.

Conclusion

A Ge-doped WO_x layer was successfully deposited on a *p*-type Si substrate by a PVD method to fabricate an Al/Si/WO_x:Ge(5.7%)/Ag heterojunction. XRD results indicate that the active layer has an amorphous and polycrystalline structure with the crystal phase of $Ge_{0.04}WO_3$, GeO_2, WO_3 and W_5O_{14}. The thickness of the active layer was observed as 435 nm from the cross-sectional SEM image. Additionally, the SEM–EDX mapping image shows that W, Ge and O are homogeneously distributed on Si wafers, with molecular weight percentage of 92.5%, 5.7% and 1.9%, respectively. In order to investigate the electrical features of the Al/Si/WO_x:Ge(5.7%)/Ag heterojunction, Ag-rectifying contacts were grown on film surfaces. The electrical properties of the Al/Si/WO_x:Ge(5.7%)/Ag heterojunction were characterised under dark and various light intensities at a ± 2 V voltage difference. Diode parameters (n, ϕ_b, R_s andI_0) were determined under dark and illumination conditions using different methods. Whilst, in general, I_0 values increase with the increase in light intensity, ϕ_b and R_s values decrease. n values show fluctuation with light intensity. At the same time, Iph, R and S values of the Al/Si/WO_x:Ge(5.7%)/Ag heterojunction were investigated depending on the light intensity under forward and reverse bias. Generally, these values increase with the increase in light intensity. Additionally, the photovoltaic parameters (Impp, Isc, Vmpp, Voc ve FF) of the Al/Si/WO_x:Ge(5.7%)/Ag heterojunction depending on light intensity were investigated, and an increase in the FF value with increasing light intensity was observed. In light of these results, it can be concluded that the fabricated heterojunction has photodiode and photovoltaic properties.

Acknowledgments The author would like to thank Nano-Optoelectronic Research Laboratories at Istanbul University and Assoc. Prof. Fahrettin Sarcan for SEM and EDX spectrums.

Funding The author received no financial support for the research, authorship, and/or publication of this article.

Data Availability The data that support the findings of this study are available from the authors upon reasonable request.

Conflict of interest On behalf of all authors, the corresponding author states that there is no conflict of interest.

References

1. C.-Y. Huang, M.-L. Chen, C.-W. Yu, T.-C. Wan, S.-H. Chen, C.-Y. Chang, and T.-Y. Hsu, Dual Functional Photo-Response for p-Si/SiO_2/n-InGaZnO Graphene Nanocomposites Photodiodes. *Nanotechnol* 29, 505202 (2018).
2. K. Kwak, K. Cho, and S. Kim, Flexible Photodiodes Constructed with CdTe Nanoparticle Thin Films and Single ZnO Nanowires on Plastics. *Nanotechnol* 22, 415204 (2011).
3. X. Tang, M.M. Ackerman, M. Chen, and P. Guyot-Sionnest, Dual-Band Infrared Imaging Using Stacked Colloidal Quantum Dot Photodiodes. *Nat. Photonics* 13, 277 (2019).
4. Q.H. Wang, K. Kalantar-Zadeh, A. Kis, J.N. Coleman, and M.S. Strano, Electronics and Optoelectronics of Two-Dimensional Transition Metal Dichalcogenides. *Nat. Nanotechnol.* 7, 699 (2012).
5. F. Sarcan, ZnO Nanoparticles-Based Vacuum Pressure Sensor. *Nanotechnology* 31, 435502 (2020).
6. C. Hahn, Z. Zhang, A. Fu, C.H. Wu, Y.J. Hwang, D.J. Gargas, and P. Yang, Epitaxial Growth of InGaN Nanowire Arrays for Light Emitting Diodes. *ACS Nano* 5, 3970 (2011).
7. X. Wang, Y. Xu, Y. Pan, Y. Li, J. Xu, J. Chen, J. Wu, Q. Li, X. Zhang, and Z. Zhao, Low-noise X-ray PIN Photodiodes Made of Perovskite Single Crystals by Solution-Processed Dopant Incorporated Epitaxial Growth. *Nano Energy* 89, 106311 (2021).
8. M.M. Koç, N. Aslan, M. Erkovan, B. Aksakal, O. Uzun, W.A. Farooq, and F. Yakuphanoğlu, Electrical Characterization of Solar Sensitive Zinc Oxide Doped-Amorphous Carbon Photodiode. *Optik* 178, 316 (2019).
9. X. Tang, G.J. Matt, S. Gao, E. Gu, O. Almora, and C.J. Brabec, Electrical-Field-Driven Tunable Spectral Responses in a Broadband-Absorbing Perovskite Photodiode. *ACS Appl. Mater. Interfaces* 11, 39018 (2019).
10. A. Mansour, Fabrication and Characterization of a Photodiode Based on 5′, 5″-dibromo-o-cresolsulfophthalein (BCP). *Silicon* 11, 1989 (2019).
11. A. Özkartal and D.T. Noori, Effects of Thermal Annealing on the Characterization of p-NiO/n-GaAs Heterojunctions Produced by Thermal Evaporation. *J. Mater. Sci: Mater. Electron* 32, 13462 (2021).
12. Z.A. Jezeh, B. Efafi, and B. Ghafary, The Effect of Electrode Shape on Schottky Barrier and Electric Field Distribution of Flexible ZnO Photodiode. *Sci. Rep.* 11, 1 (2021).
13. Ü. Doğan, F. Sarcan, K.K. Koç, F. Kuruoğlu, and A. Erol, Effects of Annealing Temperature on a ZnO Thin Film-Based Ultraviolet Photodetector. *Phys Scripta* 97, 015803 (2022).
14. F. Sarcan, S. Orchard, B. Kuerbanjiang, A. Skeparovski, V.K. Lazarov, and A. Erol, Ultraviolet Photodetector Based on Mg0. 67Ni0. 33O Thin Film on SrTiO3. *Phys. Status Solidi RRL* 14, 2000175 (2020).
15. N. Aslan, M.Ş Kurt, and M.M. Koç, Morpho-Structural and Optoelectronic Properties of Diamond Like Carbon–Germanium (DLC-Ge) Composite Thin Films Produced by Magnetron Sputtering. *Opt. Mater.* 126, 112229 (2022).
16. N. Basman, N. Aslan, O. Uzun, G. Cankaya, and U. Kolemen, Electrical Characterization of Metal/Diamond-Like Carbon/Inorganic Semiconductor MIS Schottky Barrier Diodes. *Microelectron. Eng.* 140, 18 (2015).
17. M. Gedikpınar, M. Çavaş, Z.A. Alahmed, and F. Yakuphanoglu, Electronic Properties of Al/p-Si/C70/Au MIS-type Diode. *Superlattices Microstruct.* 59, 123 (2013).
18. R. Chandiramouli and B. Jeyaprakash, Review of CdO Thin Films. *Solid State Sci.* 16, 102 (2013).

19. G. Liu, B.R. Tuttle, and S. Dhar, Silicon Carbide: A Unique Platform for Metal-Oxide-Semiconductor Physics. *Appl. Phys. Rev.* 2, 021307 (2015).
20. H. Ohta, M. Kamiya, T. Kamiya, M. Hirano, and H. Hosono, UV-Detector Based on pn-heterojunction Diode Composed of Transparent Oxide Semiconductors, p-NiO/n-ZnO. *Thin Solid Films* 445, 317 (2003).
21. Y. Tian and T. Tatsuma, Mechanisms and Applications of Plasmon-Induced Charge Separation at TiO_2 Films Loaded with Gold Nanoparticles. *J. Am. Chem. Soc.* 127, 7632 (2005).
22. H. Zhou, L. Li, H. Chen, Z. Guo, S. Jiao, and W. Sun, Realization of a Fast-Response Flexible Ultraviolet Photodetector Employing a Metal–Semiconductor–Metal Structure InGaZnO Photodiode. *RSC Adv.* 5, 87993 (2015).
23. S. Terohid, S. Heidari, A. Jafari, and S. Asgary, Effect of Growth Time on Structural, Morphological and Electrical Properties of Tungsten Oxide Nanowire. *Appl. Phys. A* 124, 1 (2018).
24. X.-T. Yin, P. Lv, J. Li, A. Jafari, F.-Y. Wu, Q. Wang, D. Dastan, Z. Shi, S. Yu, and H. Garmestani, Nanostructured Tungsten Trioxide Prepared at Various Growth Temperatures for Sensing Applications. *JALCOM* 825, 154105 (2020).
25. Z. Xu, J. Vetelino, R. Lec, and D. Parker, Electrical Properties of Tungsten Trioxide Films. *J. Vacuum Sci. Tech. A: Vacuum, Surf. Films* 8, 3634 (1990).
26. Y. Lee, S. Seo, T. Nam, H. Lee, H. Yoon, S. Sun, I.-K. Oh, S. Lee, B. Shong, and J.H. Seo, Growth Mechanism and Electrical Properties of Tungsten Films Deposited by Plasma-Enhanced Atomic Layer Deposition with Chloride and Metal Organic Precursors. *Appl. Surf. Sci.* 568, 150939 (2021).
27. G.-L. Tan, D. Tang, D. Dastan, A. Jafari, J.P. Silva, and X.-T. Yin, Effect of Heat Treatment on Electrical and Surface Properties of Tungsten Oxide Thin Films Grown by HFCVD Technique. *J. MSSP* 122, 105506 (2021).
28. H. Ji, W. Zeng, and Y. Li, Gas sensing Mechanisms of Metal Oxide Semiconductors: A Focus Review. *Nanoscale* 11, 22664 (2019).
29. H.-H. Lu, J.-P. Xu, and L. Liu, Using Ge-doped La-Oxynitride as Interfacial Passivation Layer for GaAs Metal-Oxide-Semiconductor Capacitors. *TDMR* 16, 617 (2016).
30. A. Krammer, A. Magrez, W.A. Vitale, P. Mocny, P. Jeanneret, E. Guibert, H.J. Whitlow, A.M. Ionescu, and A. Schüler, Elevated Transition Temperature in Ge Doped VO_2 Thin Films. *J. Appl. Phys.* 122, 045304 (2017).
31. B.-E. Park, Y. Lee, I.-K. Oh, W. Noh, S. Gatineau, and H. Kim, Structural and Electrical Properties of Ge-doped ZrO_2 Thin Films Grown by Atomic Layer Deposition for High-k Dielectrics. *J. Mat. Sci* 53, 15237 (2018).
32. S.M. Lee, S.J. Park, K.H. Lee, J.-S. Park, S. Park, Y. Yi, and S.J. Kang, Enhanced Photocurrent of Ge-doped InGaO Thin Film Transistors with Quantum Dots. *AppL. Phys. Lett.* 106, 031112 (2015).
33. S. Sathasivam, D.S. Bhachu, Y. Lu, N. Chadwick, S.A. Althabaiti, A.O. Alyoubi, S.N. Basahel, C.J. Carmalt, and I.P. Parkin, Tungsten Doped TiO_2 with Enhanced Photocatalytic and Optoelectrical Properties via Aerosol Assisted Chemical Vapor Deposition. *Sci. Rep.* 5, 1 (2015).
34. V. Kavitha, P. Mahalingam, M. Jeyanthinath, and N. Sethupathi, Optical and Structural Properties of Tungsten-Doped Barium Strontium Titanate. *Mater. Today: Proc.* 23, 12 (2020).
35. X. Tan, T. Yao, R. Long, Z. Sun, Y. Feng, H. Cheng, X. Yuan, W. Zhang, Q. Liu, and C. Wu, Unraveling Metal-Insulator Transition Mechanism of VO2triggered by Tungsten Doping. *Sci Rep* 2, 1 (2012).
36. F. Ünal, S. Demir, and H. Mammadov, Structural, Surface Morphological, Optical and Electrical Properties of In_xSe_y Thin Films, An Absorber Layer for Photovoltaic Cells Fabricated by M-CBD Method Using Different Variables. *Turkish J. Chem.* 45, 1761 (2021).
37. Z. Zhao, D. Morel, and C. Ferekides, Electrical and Optical Properties of tin-doped CdO Films Deposited by Atmospheric Metalorganic Chemical Vapor Deposition. *Thin Solid Films* 413, 203 (2002).
38. A. Buyukbas-Ulusan and A. Tataroglu, Electrical Characterization of Silicon Nitride Interlayer-Based MIS Diode. *J. Mater. Sci: Mater. Electron* 31, 9888 (2020).
39. T. İbrahim Hüdai, V. Özkan, and D. Ilbilge, Electrical Characteristics of p-Si/TiO_2/Al and p-Si/TiO_2-Zr/Al Schottky Devices. *Phil. Mag.* 96, 1684 (2016).
40. K. Shanmugasundaram, P. Thirunavukkarasu, M. Ramamurthy, M. Balaji, and J. Chandrasekaran, Growth and Characterization of Jet Nebulizer Spray Deposited n-type WO_3 Thin Films for Junction Diode Application. *Orient. J. Chem.* 33, 2484 (2017). https://doi.org/10.13005/ojc/330542.
41. F. Unal, M.S. Kurt, and S. Durdu, Investigation of the Effect of Light on the Electrical Parameters of Si/TiO_2 Heterojunctions Produced by Anodic Oxidation on p-type Si Wafer. *J. Mater Sci: Mater Electron.* (2022). https://doi.org/10.1007/s10854-022-08484-3.
42. H.G. Çetinkaya, H. Tecimer, H. Uslu, and Ş Altındal, Photovoltaic Characteristics of Au/PVA (Bi-doped)/n-Si Schottky Barrier Diodes (SBDs) at Various Temperatures. *Current Appl. Phys.* 13, 1150 (2013).
43. A. Shetty, B. Roul, S. Mukundan, L. Mohan, G. Chandan, K.J. Vinoy, and S.B. Krupanidhi, Temperature Dependent Electrical Characterisation of Pt/HfO_2/n-GaN Metal-Insulator-Semiconductor (MIS) Schottky Diodes. *AIP Adv.* 5, 097103 (2015).
44. H.M.J. Al-Ta'ii, V. Periasamy, and Y.M. Amin, Electronic Characterization of Au/DNA/ITO Metal-Semiconductor-Metal Diode and its Application as a Radiation Sensor. *PLOS ONE* 11, e0145423 (2016).
45. D.A. Aldemir, A. Kökce, and A.F. Özdemir, Schottky Diyot Parametrelerini Belirlemede Kullanılan Metotların Geniş Bir Sıcaklık Aralığı Için Kıyaslanması. *SAÜ Fen Bil. Enstit. D.* (2017). https://doi.org/10.16984/saufenbilder.279996.
46. M. Zurnacı, F. Ünal, S. Demir, M. Gür, N. Şener, and İ Şener, Synthesis of a New 1, 3, 4-Thiadiazole-Substituted Phenanthroimidazole Derivative, its Growth on glass/ITO as a Thin Film and Analysis of Some Surface and Optoelectronic Properties. *N. J. Chem.* 45, 22678 (2021).
47. S.K. Cheung and N.W. Cheung, Extraction of Schottky Diode Parameters from Forward Current-Voltage Characteristics. *Appl. Phys. Lett.* 49, 85 (1986).
48. V. Rajagopal Reddy, C. Prasad, V. Janardhanam, and C.-J. Choi, Electrical and Carrier Transport Properties of Ti/α-amylase/p-InP MPS Junction with a α-amylase Polymer Interlayer. *J. Mater. Sci. Mater.: Electron* 32, 1 (2021).
49. F. Ünal, Investigation of Some Optical and Electrical Properties of InSe Thin Film, A Window Layer for Photovoltaic Cell Growth on Glass/GaSe Substrate by M-CBD Method. *Black Sea J. Sci.* 11, 297 (2021).
50. T.U. Kampen, S. Park, and D.R.T. Zahn, Barrier Height Engineering of Ag/GaAs(100) Schottky Contacts by a Thin Organic Interlayer. *Appl. Surf Sci* 190, 461 (2002).
51. H. Uslu, Ş Altındal, İ Polat, H. Bayrak, and E. Bacaksız, On the Mechanism of Current-Transport in Cu/CdS/SnO_2/In–Ga Structures. *JALCOM* 509, 5555 (2011).
52. A. Tataroğlu, Ş Altındal, and Y. Azizian-Kalandaragh, Comparison of Electrical Properties of MS and MPS Type Diode in Respect of (In2O3-PVP) Interlayer. *Phys. B: Cond. Matter* 576, 411733 (2020).
53. R. Şahingöz, H. Kanbur, M. Voigt, and C. Soykan, The Determination of Interface States and Series Resistance Profile of Al/

polymer/PEDOT-PSS/ITO Heterojunction Diode by I-V and C-V Methods. *Synth. Metals* 158, 727 (2008).
54. Y.S. Ocak, M. Kulakci, T. Kiliçoğlu, R. Turan, and K. Akkiliç, Current-Voltage and Capacitance-Voltage Characteristics of a Sn/Methylene Blue/p-Si Schottky Diode. *Synth. Metals* 159, 1603 (2009).
55. E.H. Rhoderick, Metal-Semiconductor Contacts. *IEE Proc. I-Solid-State Electron Devices* 129, 1 (1982).
56. T. Tunç, Ş AltIndal, I. Dökme, and H. Uslu, Anomalous Peak in the Forward-Bias C-V Plot and Temperature-Dependent Behavior of Au/PVA (Ni, Zn-doped)/n-Si(111) Structures. *JEM* 40, 157 (2011).
57. H.C. Card and E.H. Rhoderick, Studies of Tunnel MOS Diodes I. Interface Effects in Silicon Schottky Diodes. *J. Phys. D: Appl. Phys* 4, 1589 (1971).
58. S. Demirezen and S. Altindal, Possible Current-Transport Mechanisms in the (Ni/Au)/$Al_{0.22}Ga_{0.78}N$/AlN/GaN Schottky Barrier Diodes At The Wide Temperature Range. *Current Appl. Phys.* 10, 1188 (2010).
59. P. Chattopadhyay and B. RayChaudhuri, Frequency Dependence of Forward Capacitance-Voltage Characteristics of Schottky Barrier Diodes. *Solid State Elect.* 36, 605 (1993).
60. A. Kocyigit, M. Yılmaz, Ü. İncekara, Y. Şahin and Ş Aydoğan, The Light Detection Performance of the Congo Red Dye in a Schottky Type Photodiode. *Chem. Phys. Lett.* 800, 139673 (2022).
61. A. Farag, Structure and Transport Mechanisms of Si/porous Si n–p Junctions Prepared by Liquid Phase Epitaxy. *Appl. Surface Sci.* 255, 3493 (2009).
62. R. Tung, Electron Transport at Metal-Semiconductor Interfaces: General Theory. *Phys. Rev. B* 45, 13509 (1992).
63. W.F. Reus, M.M. Thuo, N.D. Shapiro, C.A. Nijhuis and G.M. Whitesides, The SAM, Not the Electrodes, Dominates Charge Transport in Metal-Monolayer//Ga_2O_3/Gallium–Indium Eutectic Junctions. *ACS Nano* 6, 4806 (2012).
64. X. Zhang, X. Zhang, L. Wang, Y. Wu, Y. Wang, P. Gao, Y. Han and J. Jie, ZnSe Nanowire/Si p-n Heterojunctions: Device Construction and Optoelectronic Applications. *Nanotechnology* 24, 395201 (2013).
65. B. Gündüz, N. Turan, E. Kaya and N. Çolak, The Photo-Electrical Properties of the p-Si/Fe(II)–polymeric Complex/Au Diode. *Synth. Metals* 184, 73 (2013).
66. A. Patel, P. Pataniya, G.K. Solanki, C.K. Sumesh, K.D. Patel and V.M. Pathak, Fabrication, Photoresponse and Temperature Dependence of n-VO_2/n-$MoSe_2$ Heterojunction Diode. *Superlattices Microstruct.* 130, 160 (2019).
67. B. Gündüz, I.S. Yahia and F. Yakuphanoglu, Review Article: Electrical and Photoconductivity Properties of p-Si/P3HT/Al and p-Si/P3HT:MEH-PPV/Al Organic Devices: Comparison Study. *Microelectron. Eng.* 98, 41 (2012).

Publisher's Note Springer Nature remains neutral with regard to jurisdictional claims in published maps and institutional affiliations.